Research Paper

Advances in Structural Engineering

Secondary debris resulting from concrete slabs subjected to contact detonations

Advances in Structural Engineering
2022, Vol. 25(7) 1373–1385

DOI: 10.1177/13694332221080614
journals.sagepub.com/home/ase
SAGE

Moritz Hupfauf[1] **and Norbert Gebbeken**[1]

Abstract

As a consequence of terrorist attacks with explosives and malfunction of machinery detonations can lead to secondary debris on the protective side of a concrete wall. The term secondary debris in this context describes the debris resulting from a breakup of the loaded concrete structure in contrast to primary debris which results from the explosive or its casing. A test series has been conducted in order to investigate the physical phenomenology of the damaging process. A total of 15 reinforced concrete slabs with scaled thicknesses between 1.6 and 2.8 cm $g^{-1/3}$ were loaded by contact detonations. The protective side of the concrete slabs was recorded with high-speed cameras during testing, and the damaged concrete slabs were measured with 3D-scans afterward. The acquired data will be evaluated for the velocity and mass of the secondary debris, to build the basis for an empirical model, which can make predictions about the occurring secondary debris. The objective of this paper is, to present the conducted experiments and propose the first part of an empirical model. This model predicts the geometry of the spalling crater on the protective side of the concrete slab, as well as the maximum velocity of the secondary debris. In following papers, the correlation between the mass and the velocity of the secondary debris will be derived from numerical simulations. With this, predictions can be made about the effects of the secondary debris on humans and installations on the protective side of the concrete slabs.

Keywords

contact detonation, secondary debris, concrete, spalling damage, empirical model, feature tracking, 3D-Scan

Introduction

Fragmentation of concrete structures resulting from high-speed loading events, like, explosions and impact, is an ongoing field of research. Possible scenarios for this kind of loading are terrorist attacks with explosives, but also accidents caused by malfunctions of machinery or human error. The resulting secondary debris at the protective side of a concrete wall can injure or kill people, damage technical installations of facilities, and compromise the integrity of their components.

In contrast to near-field and far-field detonations, the reaction of a structure loaded by a contact detonation is dominated by a very localized damage. The global response of the structure will not be affected. The pressure generated by the explosive is directly transmitted into the structure. There, it induces a hemispherical expanding shock wave (Tu et al., 2019). As a consequence of the hemispherical propagation of the shock wave, the total energy disperses over the length of the expanding shock wave (McVay, 1988). The work the shock wave does on the material transforms the induced energy to energy forms in connection with heat, pore crushing, and the generation of cracks (attenuation, Meyers, 1994). Both, the dispersion and the energy transformation effects decrease the amplitude of the shock wave during its propagation inside of the concrete. As long as the resulting hydro-static pressure in the concrete exceeds its hugoniot elastic limit, the concrete is crushed and a crater is formed (Gebbeken and Krauthammer, 2013).

When the pressure wave reaches the back of the concrete slab, it is reflected at the free surface as a tensile wave. The reflected tensile wave superimposes with the remaining part of the incoming pressure wave. As soon as the resulting stress causes a tensile stress above the dynamic tensile strength of the concrete, a tensile crack is formed (McVay, 1988). This results in spalling (fragmentation of

[1]University of the Bundeswehr Munich, Neubiberg, Germany

Corresponding author:
Moritz Hupfauf, Universität der Bundeswehr München Fakultät für Bauingenieurwesen und Umweltwissenschaften, Institute of Engineering Mechanics and Structural Analysis, Werner-Heisenberg-Weg 39, Neubiberg 85577, Germany.
Email: moritz.hupfauf@unibw.de

Table 1. Overview of the test series.

Name (shot nr.)	Explosive mass (SEMTEX 10)	Slab thickness
SN80	1500 g	20 cm
SN82	1500 g	25 cm
SN128	1500 g	25 cm
SN129	1000 g	20 cm
SN130	2000 g	25 cm
SN131	1000 g	30 cm
SN132	1000 g	30 cm
SN142	1000 g	20 cm
SN143	1500 g	30 cm
SN144	2000 g	25 cm
SN145	1500 g	30 cm
SN146	2000 g	30 cm
SN147	2000 g	30 cm
SN174	1500 g	20 cm
SN175	1000 g	25 cm

concrete) on the protective side of the reinforced concrete slab. In this test series, the location of the cracks was often in the plane of the reinforcement. This can be explained by multiple reflections on the different surfaces in this area, which can lead to a premature failure. As soon as the crushing crater (compression failure) and the spalling crater (tensile failure) overlap, a breach occurs (Figure 9).

The spalled debris has a momentum, which is caused by the impulse of the shock wave trapped between the free surface and the crack, minus the impulse of the restive forces of the concrete (McVay (1988)). A good overview of the theoretical background can be found in Meyers (1994) and Hiermaier (2008).

An extensive study about the spalling of concrete structures loaded by airblast and bomb fragments was conducted by McVay (1988). McVay presents and evaluates a test series for the influence of different parameters like concrete thickness, explosive mass, and reinforcement. He also compares different theoretical and empirical methods for the prediction of spalling. An analytical model to predict the compressive damage of concrete plates under contact detonations was developed by Tu et al. (2019). A more recent test series regarding the spalling damage of normal and ultra-high-strength concrete under contact detonations was conducted by Li et al. (2015) and compared with numerical methods.

To get a deeper insight into the mechanics of the secondary debris resulting from reinforced concrete slabs loaded by contact detonations, a test series has been conducted by the research group BauProtect. The reinforced concrete slabs had outer dimensions of 200 cm × 200 cm and varying thicknesses between 20 cm and 30 cm (Table 1). The explosives were cylindrical charges with a mass between 1000 g and 2000 g of SEMTEX 10.

During testing, the protective side of the concrete slabs was recorded with high-speed cameras. The recordings have been evaluated with respect to the velocity of the secondary debris as well as the breakup process. After testing, the damaged areas of the concrete slabs were measured with 3D-scans, and the secondary debris was collected by hand and vacuum cleaner. Subsequently, the collected debris was sieved and weighed. These data have then been evaluated with respect to the geometry of the spalling crater as well as the mass and size distribution of the secondary debris.

Similar tests with high-speed recordings of the protective side of the concrete slab were conducted by Bewick (2017) and Shi et al. (2020). Bewick tested 5 cm thick concrete slabs without reinforcement loaded by a shock tube. Shi et al. tested 12 cm thick reinforced concrete slabs with blast loads between 2 kg and 6 kg TNT at a standoff distance of 40 cm. Both authors measured the velocity as well as the mass and size distribution of the secondary debris. A statistical description of the debris throw resulting from a detonation inside of a ammunition storage was conducted by Van der Voort and Weerheijm (2013). A test series with contact charges on normal concrete and ultra-high-strength concrete slabs was conducted by Li et al. (2016). They compared the observed crushing crater and spalling crater damage to existing empirical models and fitted the resulting fragment size distributions with different statistical distributions. To the knowledge of the author, no experiments have been conducted yet, where concrete slabs were loaded by contact charges and evaluated with respect to the velocity of the resulting secondary debris.

Experimental setup

The goal of this test series is to investigate the secondary debris on the protective side of a concrete slab resulting from contact detonations. Table 1 gives an overview of all the conducted tests relevant for this paper in chronological order. The missing shot numbers are a result of additional tests, which are not part of this paper. Those tests include the usage of steel fiber reinforced concrete and other external reinforcements, like micro-reinforced ultra-high-strength concrete and aluminum foam, to evaluate their ability to reduce the occurring secondary debris. They will be presented in following papers.

The concrete slabs were prepared by a commercial manufacturer. At the day of testing, all concrete slabs had an age of at least 25 days but on average 80 days. The static compressive strength and density of the concrete were measured for each concrete slab on three associated test cubes with an edge length of 15 cm. The concrete had an average static compressive strength (cube) of 42.9 ± 4.2 MPa, an average density of 2.22 ± 0.03 g cm^{-3} (mean ± standard deviation) and a water-cement-ratio of 0.44. The

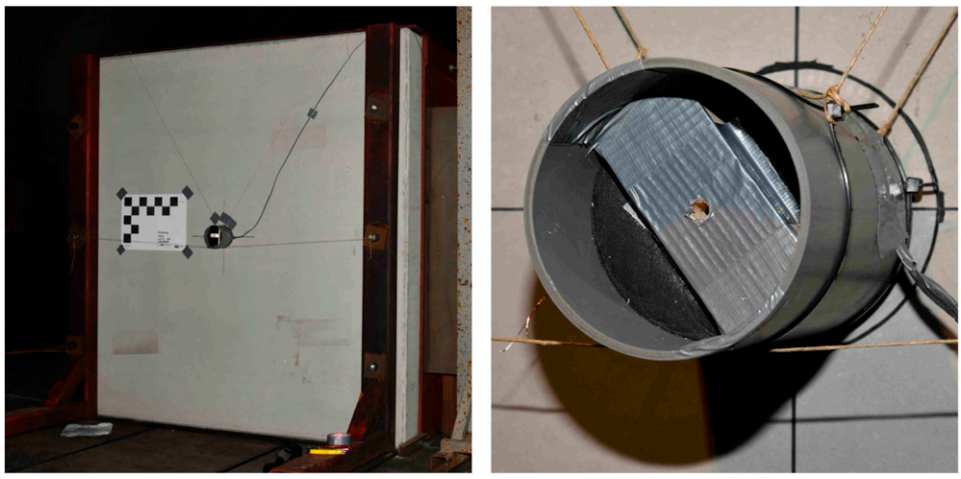

Figure 1. Experimental setup from detonation side (left) and detail explosive (right).

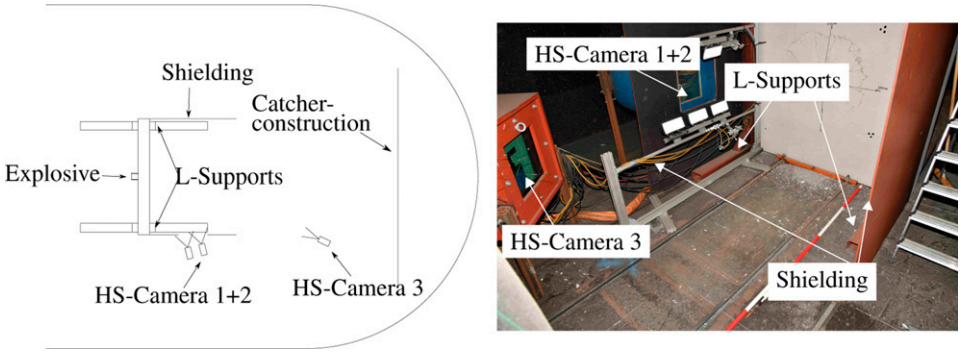

Figure 2. Experimental setup in layout (left) and photo (right).

grain size was distributed with 48.9% below 2 mm and 51.1% between 2 and 8 mm. The reinforcement for all concrete slabs was a high ductility steel B500B with a diameter of 10 mm and a spacing of 150 mm. The reinforcement was laid crosswise on both surfaces with a concrete covering of 35 mm.

The employed explosive was SEMTEX 10. After weighing, the explosive was molded into a PVC-pipe with a circular cross section and an inner diameter of 103 mm. The explosive was attached flush with the flat surface of the cylinder to the center of the surface of the concrete slab. The resulting height to diameter ratios (explosive without PVC-pipe) of the different charges were 0.7 for 1000 g, 1.1 for 1500 g and 1.5 for 2000 g. The charges were ignited with a Dynadet-C2-Detonator, which was pressed 10 mm deep into the center of the surface of the explosive opposite to the concrete slab. Figure 1 shows the experimental setup from the detonation side as well as a detail of the prepared explosive.

The tests were conducted in a bunker at a facility of the Netherlands Organization for Applied Scientific Research (TNO) near The Hague. The cross-section of the oblong bunker has approximate dimensions of 6 m in width and 4 m in height. The experimental setup is depicted in Figure 2.

The reinforced concrete slabs were held in an upright position by L-shaped steel beams. These 20 cm wide steel beams (L-supports) were placed in front of both surfaces of the concrete slabs, and held together with threaded steel rods. The resulting horizontal clearance between the steel beams was 160 cm. The dimensions of the test specimens were chosen, such that the influence of the support conditions is negligible for the relevant localized reaction of the concrete slab.

The protective side of the test specimens was recorded by high-speed-cameras (HS-cameras) from different angles. HS-cameras 1 + 2 recorded from the side and covered an area up to a horizontal distance of

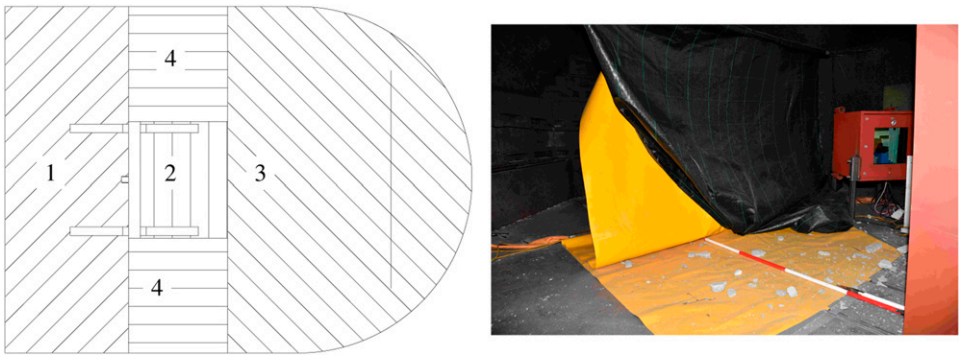

Figure 3. Areas for collection of secondary debris (left), curtain construction to stop the secondary debris (right).

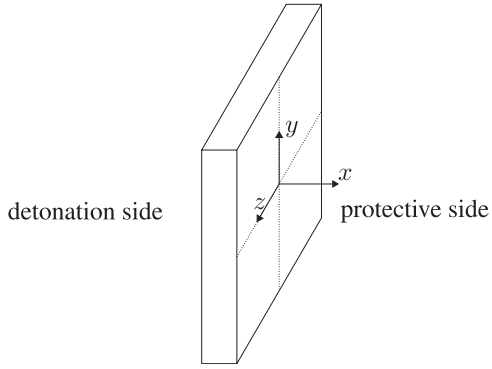

Figure 4. Coordinate system for the evaluation of the measurements.

110 cm behind the concrete slab. HS-camera 3 recorded the surface of the protective side of the concrete slab during breakup. The HS-cameras where placed inside of steel boxes with armored glass windows to protect them from the detonation. An additional steel shielding was installed behind the concrete slab, to minimize a negative influence of the detonation on the HS-recordings. All HS-recordings were done with a frequency of 5000 s^{-1}. The resolution of the HS-recordings resulted in a precision of approximately 1.8 mm px^{-1}. The recordings were started before the detonation, and got the information about the time of detonation from a trigger which was fixed to the surface of the explosive.

To stop the resulting debris as gently as possible, and prevent additional breakup of the debris, a curtain construction was installed at a distance of approximately 4 m behind the concrete slab. After the detonation the resulting debris was collected by segmental areas. Figure 3 shows the different collecting areas as well as the curtain construction.

Measurements

The following section will describe the evaluation of the conducted measurements. For the description of the measurements, a Cartesian coordinate system with its origin at the center of the surface of the protective side of the concrete slab will be used (Figure 4). The x-axis of this coordinate system is parallel to the normal vector of the concrete surface and the y-axis points upwards.

All conducted regression analyses have been calculated with a least-square approach.

High-speed recordings

The analysis of the high-speed recordings was performed with help of the open source library OpenCV. Information about the implemented algorithms can be found in the literature (Hartley and Zisserman, 2004; Kaehler and Bradski, 2016; Schreer, 2005; Szeliski, 2010).

HS-cameras 1+2 were oriented at a horizontal angle of approximately 75° relative to the x-axis. In order to perform measurements in the HS-recordings, the perspective of the image plane was transformed into a target plane, so that distances and angles are represented correctly in this target plane ($x - y - plane$, $z = 0$, target plane of HS-cameras 1+2). Marks on the surface of the concrete slabs with known relative coordinates were used as a reference for the determination of the corresponding homography and scale. The same procedure was used for HS-camera 3 with the difference, that the target plane of the transformation was located in the surface of the concrete slab ($y - z - plane$, $x = 0$, target plane of HS-camera 3).

It should be noted, that in the resulting HS-images only those distances are displayed correctly, which lie exactly in the target plane of the associated transformation. All distances which lie in front or behind this target plane, will be displayed too long or too short according to the intercept theorem. For this reason, the tip of the debris cloud in Figure 5 (left) appears to be shifted to the right, since it is no

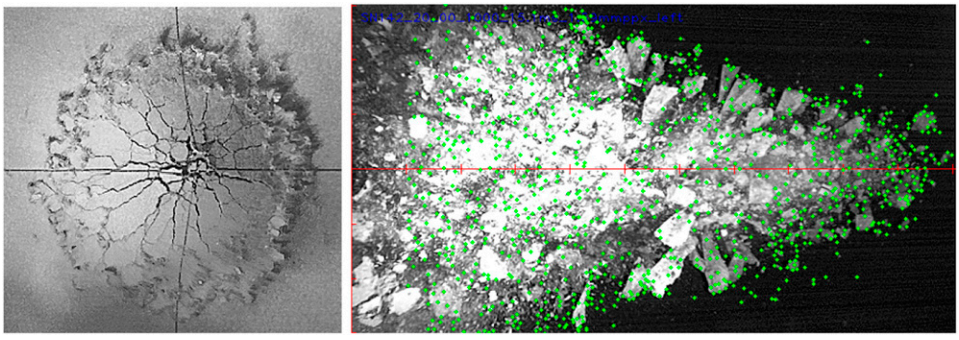

Figure 5. Spalling of the concrete at 1.4 ms (left) and tracking at 15.1 ms (right)—SN142.

longer located in the associated target plane ($y - z - plane$, $x = 0$).

The resulting maximum error of the distance measurements from HS-camera 1+2 can be estimated on the basis of the rotational symmetry of the debris cloud. For example, the radial dimension of the debris cloud in test SN142 (Figure 5) has a diameter of approximately 60 cm. With the known distance of 120 cm between the associated target plane ($x - y - plane$, $z = 0$) and the HS-camera, the maximum error of the distance measurements is ±25%. Because the debris cloud in this test is very dense, debris which is behind the target plane ($x - y - plane$, $z = 0$) is less likely to be tracked. Therefore, the measured distances are more likely to be too short and as a consequence the derived velocities are too slow. At the tip of the debris cloud, the error of the measured distances is considerably smaller, because the debris is closer to the target plane ($x - y - plane$, $z = 0$).

To determine the velocities of the secondary debris, a tracking algorithm was applied to the transformed recordings of HS-camera 1+2. This algorithm detects characteristic features and follows these features between the different time steps with the help of optical flow (Bouguet, 1999; Lucas and Kanade, 1981). A feature in this context describes unique patterns of neighboring pixels, which are based on their respective color and brightness values, and can be allocated in different pictures. For added robustness, an expected search location for a feature in the following time step is prescribed based on the velocity and direction of movement of the respective feature in the preceding time steps. During tracking, the algorithm constantly checks the quality of the matched features in consecutive time steps. This is done by applying the optical flow algorithm backwards and comparing the position of the same feature from both directions in the same time step. If the calculated distance is bigger than one pixel, the feature is discarded from further tracking. In addition, the algorithm checks for new characteristic features in every fifth time step (1.0 ms) and adds them to the list of tracked features. Beside the negative influences of light and dust, the shaking of the HS-cameras causes a challenge for the tracking algorithm. As a measure against this, the velocities of the debris are averaged over all preceding time steps. To exclude a tracking of parts in the background, features with a velocity in x-direction smaller than 0.1 ms are discarded, and the search area is restricted by a mask. To exclude a tracking of stirred up dirt not resulting from the concrete slab, features with a movement outside of three times the standard deviation of the movement of all features in the same time step are discarded. Figure 6 shows a flowchart for the tracking algorithm.

The tracking algorithm works much better for dense debris clouds than for sparse debris clouds. In the case of sparse debris clouds, parts of the background have a much stronger influence on the quality of tracking. Figure 5 (right) shows an example of the recordings of HS-camera 1 as well as the tracked features (dots).

Tests SN80-SN82 were part of a pretest series with a slightly different test setup. The main difference was a 10 cm wide, vertical slit construction at a horizontal distance of 100 cm behind the concrete slab. The goal of this was, to reduce the debris cloud to a smaller lateral dimension, to ensure a more precise distance between the HS-camera and the tracked features. But, this slit construction disturbed the flight of the resulting debris too much, and was therefore removed from the main test series. In the first pretest SN80, the high-speed recordings were not successful, and therefore no tracking could be conducted. Because of a slightly different setup, the tracking of SN82-SN129 was done by manual tracking of only a small number of fragments with help of the Open Source Physics Software Tracker.

Figure 7 (left) shows the measured maximum x-velocities of the secondary debris over the scaled thickness of the concrete slab. The scaling is achieved by dividing the slab thickness through the cube root of the TNT-equivalent explosive mass. The TNT-equivalence-factor for SEMTEX 10, which is based on the heat of

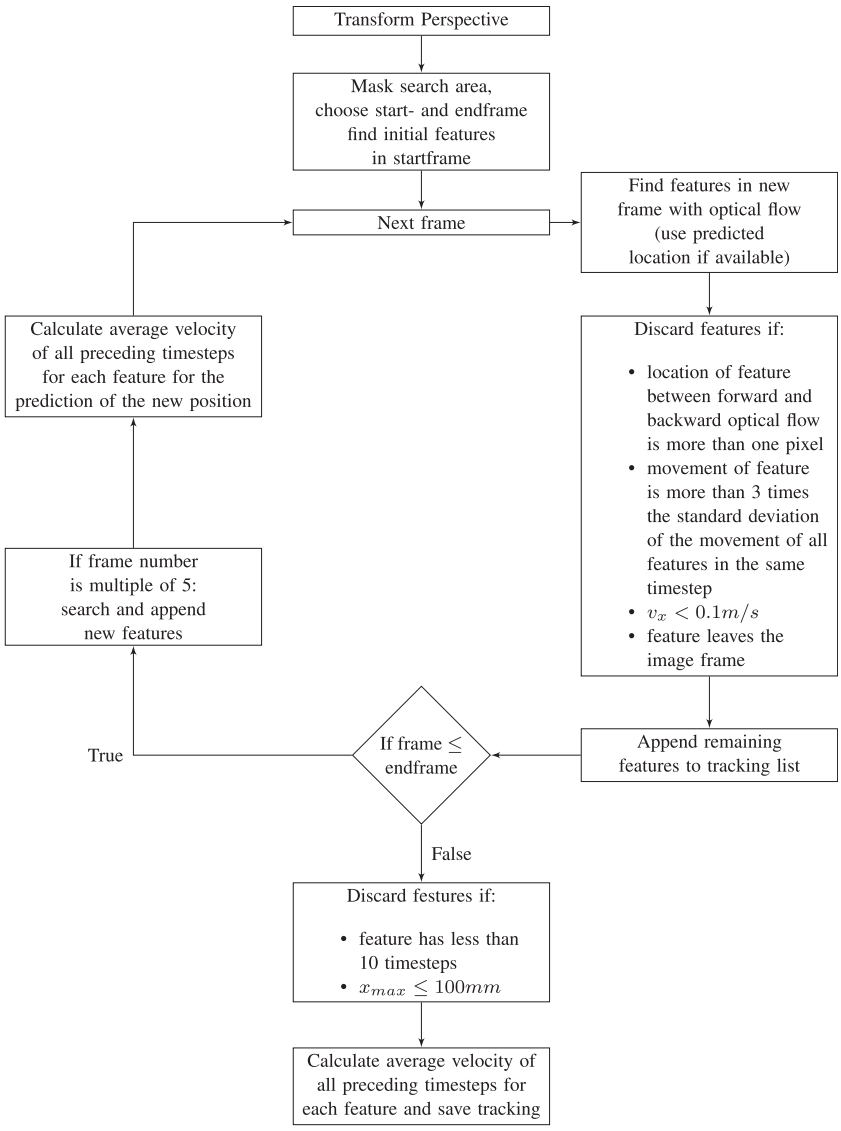

Figure 6. Flowchart for the tracking algorithm.

detonation, was set to 1.25 in accordance with Shirbhate and Goel (2021). The maximum x-velocity for all tests can be approximated with a quadratic regression over the scaled thickness. For smaller scaled thicknesses, the debris has a larger maximum x-velocity, which gets smaller with an increasing scaled thickness.

To get some information about the flight direction, Figure 8 (left) shows the angle of the resulting velocity ($v_x + v_y$) for the tracked features of SN142 relative to the *x*-axis, as well as a linear regression. Because of the rotational symmetry of the debris cloud around the *x*-axis, the velocity in *y*-direction can be interpreted as a radial velocity. This shows, that the movement of the debris is dominant in the *x*-direction because the majority of the debris moves at an angle smaller than 20% relative to the *x*-axis. This equals to a velocity in radial direction smaller than 50% of the velocity in *x*-direction. This trend can be observed for all tests in a similar way. Figure 8 (right) shows the resulting regression lines for all tests as well as an averaged regression line. It would be expected, that all regression lines go through the origin ($y = 0$, $angle = 0$) of the coordinate system. This discrepancy can be explained by a non-symmetric distribution of the tracked features, as well as imperfections due to shaking and a slight deviation of the main flight direction from the *x*-axis. The rather bigger slope of the regression line for SN145 can be explained by a big rotating debris part. This results in a bigger tracked velocity in *y*-direction which is not caused by a translational movement.

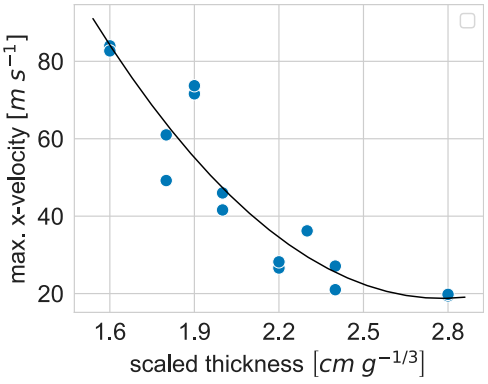

Figure 7. Maximum x-velocity of the debris over the scaled thickness.

crater, breach, and spalling crater. Figure 9 shows these areas as well as the associated dimensions.

In Figure 9, the explosive and the crushing crater (compressive damage) are on the bottom and the spalling crater (tensile damage) on top of the concrete slab. The breach is the location of the narrowest opening, and represents the geometric transition between the crushing crater and the spalling crater. The left figure shows the situation without a breach and the right figure the situation with a breach. The dimensions of the crushing crater, spalling crater and breach are approximated by equivalent circles and their associated radii. To take the hemispherical propagation of the shock wave in the concrete slab into account, the radii of the spalling crater and the breach can be expressed in dependence on the spalling crater angle α

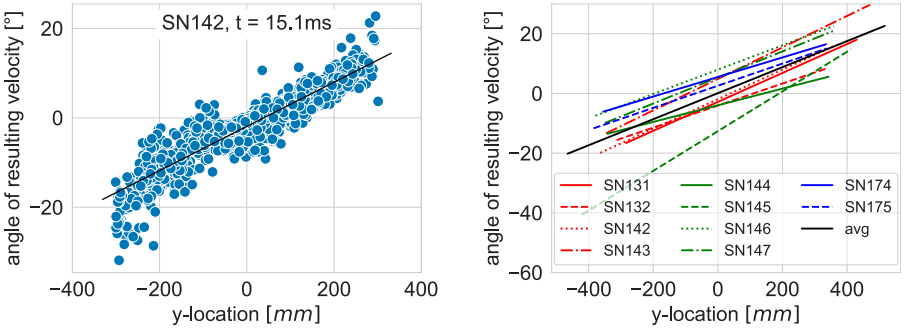

Figure 8. Angle of resulting velocity ($v_x + v_y$): measured values including regression line for SN142, t = 15.1 ms (left) and regression lines for all shots (right).

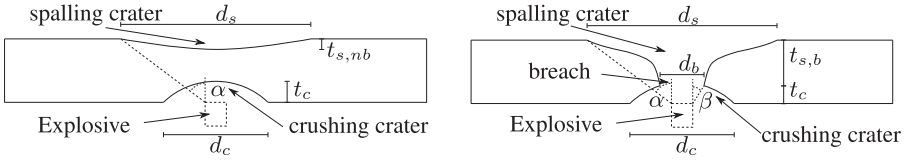

Figure 9. Dimensions of the damaged areas without breach (left) and with breach (right); *d* = diameter, *t* = depth, *c* = crushing crater, *b* = breach, *nb* = no breach, *s* = spalling crater, α = spalling crater angle, β = breach angle.

It is important to note, that these measurements cannot be used to draw a conclusion about the mass-velocity-distribution. The measured velocities represent the tracked features, which have only a rough correlation with the corresponding mass, because the density of the debris cloud is unknown.

Damaged areas

The evaluation of the visible damaged areas of the concrete slabs is done separately for the different areas: crushing

and the breach angle β. These angles are defined as the angles between the *x*-axis and the line which connects the outer edge of the explosive on the surface of the concrete slab with the radii of the breach or the spalling crater at the associated locations (Figure 9).

An important influence on the secondary debris is whether a breach of the concrete slab occurs or not. In the present test series, a breach occurs for all tests with a scaled thickness smaller than 2.2 cm $g^{-1/3}$. In all tests with a scaled thickness bigger than or equal to 2.2 cm $g^{-1/3}$ no breach and only spalling can be observed on the protective

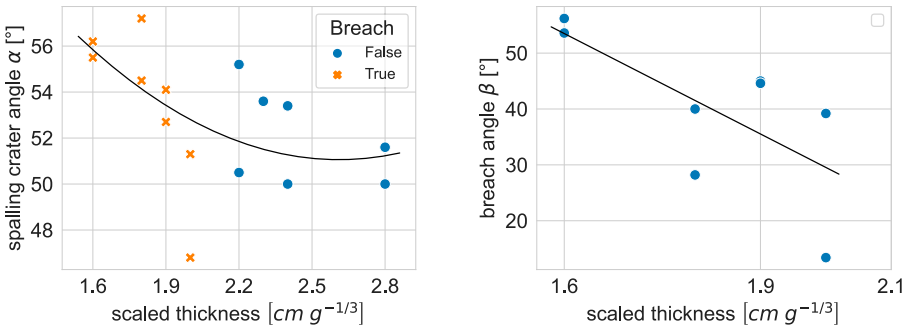

Figure 10. Correlation between the explosive mass (SEMTEX10) and the diameter (left) and depth (right) of the crushing crater.

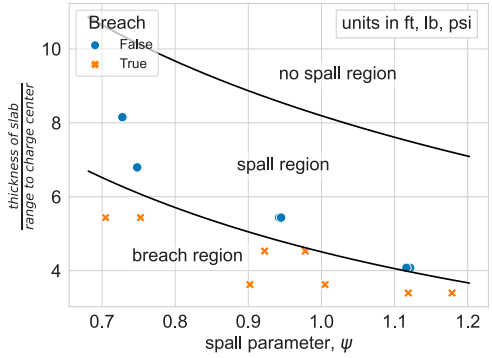

Figure 11. Scanned points of spalling crater projected into y-z-plane (gray dots) with averaged dimensions for breach and spalling crater (red lines)—SN142 (number of points reduced for plot).

side of the concrete slab. Figure 10 (left) shows the occurrence of a breach in dependence on the scaled thickness.

To compare the results of the conducted test series with existing data in the literature, they are compared with the damage that is predicted by UFC 3-340-02 (DoD (2008)). UFC 3-340-02 gives threshold curves for concrete spalling and breach (eq. 4-178 & 4-179), that are calculated based on the spall-parameter ψ and the thickness of the concrete slab in relation to the distance between the center of the charge and the surface of the concrete slab. In this context, the TNT-equivalence-factor for SEMTEX 10 is 1.25 (Shirbhate and Goel, 2021) and the burst configuration factor B_f was set to 0.75 to fit the present data. All remaining factors were set according to UFC 3-340-02. It is important to note, that since the factors of the underlying formulas are of empirical nature, imperial units are used in accordance with UFC 3-340-02. Figure 11 shows the resulting threshold curves (solid lines) as well as the results of our conducted tests ("×", "•"). A good agreement can be observed regarding the occurring damage.

The areas of the crushing craters at the surfaces of the concrete slabs were measured in photos, that were taken directly after the tests. These photos were transformed into the y-z-plane of the concrete slab surface (x=0) in the same manner like the HS-recordings. The measured areas of the crushing craters at the surfaces of the concrete slabs are transformed into an area equivalent circle with a respective diameter. The depths of the crushing craters were measured in the center of the damaged area directly after testing with a folding rule. Figure 12 shows the diameter (left) and the depth (right) of the crushing craters for all test in dependence on the explosive mass including linear regression lines. For the depth of the crushing crater, two separate regression lines are drawn in dependence on the occurrence of a breach.

For 1000 g of explosive (SEMTEX 10), there is a big variation in the measured diameters. This variation gets smaller with an increasing explosive mass (SEMTEX 10). The average size of the crushing crater in diameter and depth grows with an increasing explosive mass (SEMTEX 10). When a breach occurs, it is located at the transition from crushing crater to spalling crater at a crushing crater depth t_c of approximately 6.5 cm for all cases.

To evaluate the shape of the spalling crater, the tested slabs were measured with 3D-Scans. The coordinates of all scanned points from the 3D-Scans were transformed into cylindrical coordinates with the x-axis as the axis of rotation. The location of the origin of the coordinate system is calculated as the center of all scanned points of the spalling crater projected to the surface of the undamaged concrete slab ($x = 0$). The radii of the spalling crater and the breach are given as the averaged radii of the scanned points at the surface of the concrete slab ($x = 0$) and the location of the breach ($x = -t_s$), respectively. Figure 13 shows an example of the scanned points projected into the y-z-plane (gray dots) including the averaged dimensions for breach and spalling crater (red lines).

Figure 10 shows the angles for breach and spalling crater, which have been introduced in Figure 9, in

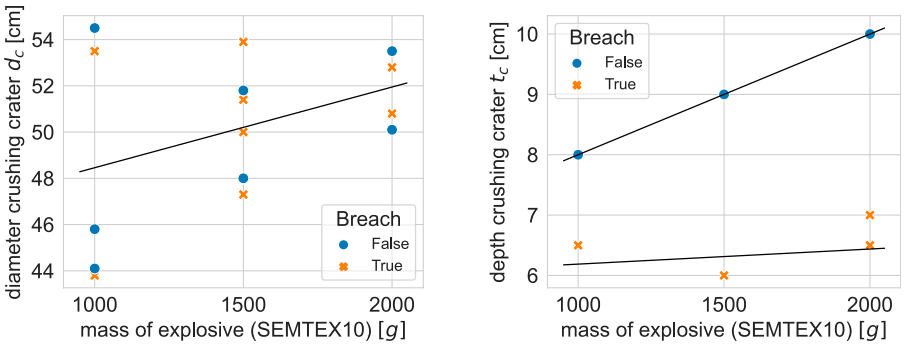

Figure 12. Spalling crater angle (left) and breach angle (right) over scaled thickness.

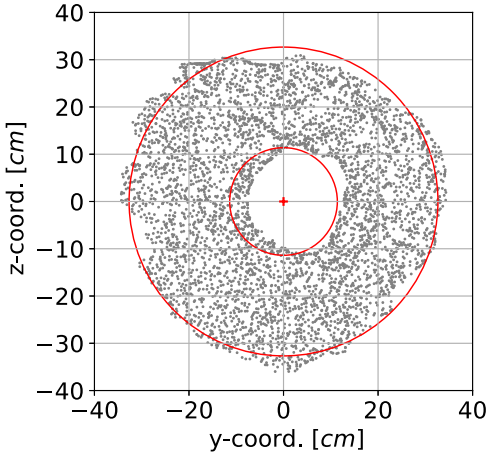

Figure 13. Conducted tests (dots and crosses) and damage threshold curves (solid lines) according to UFC 3-340-02 DoD (2008).

dependence on the scaled thickness for all tests including regression lines. The regression line for the spalling crater angle α is quadratic and the regression line for the breach angle β is linear.

For both angles (spalling crater and breach) a decreasing trend can be observed regarding an increasing scaled thickness up to the threshold for the occurrence of a breach (scaled thickness $>$ 2.2 cm g$^{-1/3}$). The smaller angles for bigger scaled thicknesses can be explained by a stronger attenuation of the pressure wave, as a consequence of the longer path it has to travel through the concrete. As soon as a breach occurs (scaled thickness $\geq$2.2 cm g$^{-1/3}$), the slope of the regression line for the spalling crater angle is considerably smaller. A reason for the comparably small spalling crater angle of 47° at a scaled thickness of 2.0 cm g$^{-1/3}$ (SN82) could not be found.

To evaluate the 3D-shape of the spalling crater, the scanned points of the spalling crater in cylindrical coordinates, were rotated around the x-axis into one common radius-depth-plane separate for each test. The average positions of these points were then approximated by higher order polynomials. The endpoints of these polynomials were fixed to the determined radii of the breach and the spalling crater at the surface of the concrete slab (x = 0). Figure 14 shows an example of the scanned points projected into the x-y-plane (gray dots), transformed into cylindrical coordinates and depicted in the radius-depth-plane (black dots) including an approximation by a higher order polynomial (red line).

Figure 15 shows the resulting polynomials of the averaged shapes of the spalling craters for all tests (solid and dashed lines). The upper four diagrams show the tests with a breach, and the lower four diagrams show the tests without a breach.

Figure 15 also shows empirical approximations (dash-dotted lines), which are based on the conducted regression analysis for the spalling crater angle and the breach angle. These approximations are defined by three points: the radius of the breach (A), the radius of the spalling crater (C) and the radius at the plane of the reinforcement (B) (Figure 16).

The radii of spalling crater and breach are calculated with the regression lines for the associated angles based on the scaled thickness (Figure 10). The threshold for the occurrence of a breach is a scaled thickness smaller than 2.2 cm g$^{-1/3}$. Like observed in the conducted tests (Figure 12, right), the breach is at a mean measured crushing crater depth of t_c = 6.5 cm. For all tests without a breach, the average depth of the spalling crater is directly beneath the reinforcement (Figure 15). For the present cases, with a concrete covering of 3.5 cm and two layers of rebar with a diameter of 10 mm, this depth equals to ts,nb = 5.5 cm. The radius at the plane of the reinforcement is calculated with the average angle for the spalling crater and the breach ($\gamma = (\alpha + \beta)/2$). For the calculation of γ in all cases without a breach, the angle β is set to a constant value resulting from the threshold scaled thickness of 2.2 cm g$^{-1/3}$.

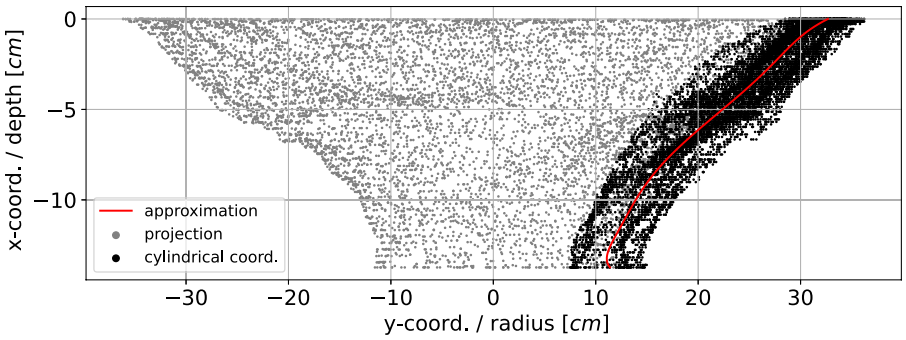

Figure 14. Scanned points of spalling crater projected into x-y-plane (gray dots) transformed into cylindrical coordinates and depicted in the radius-depth-plane (black dots) including an approximation by a higher order polynomial (red line)—SN142 (number of points reduced for plot).

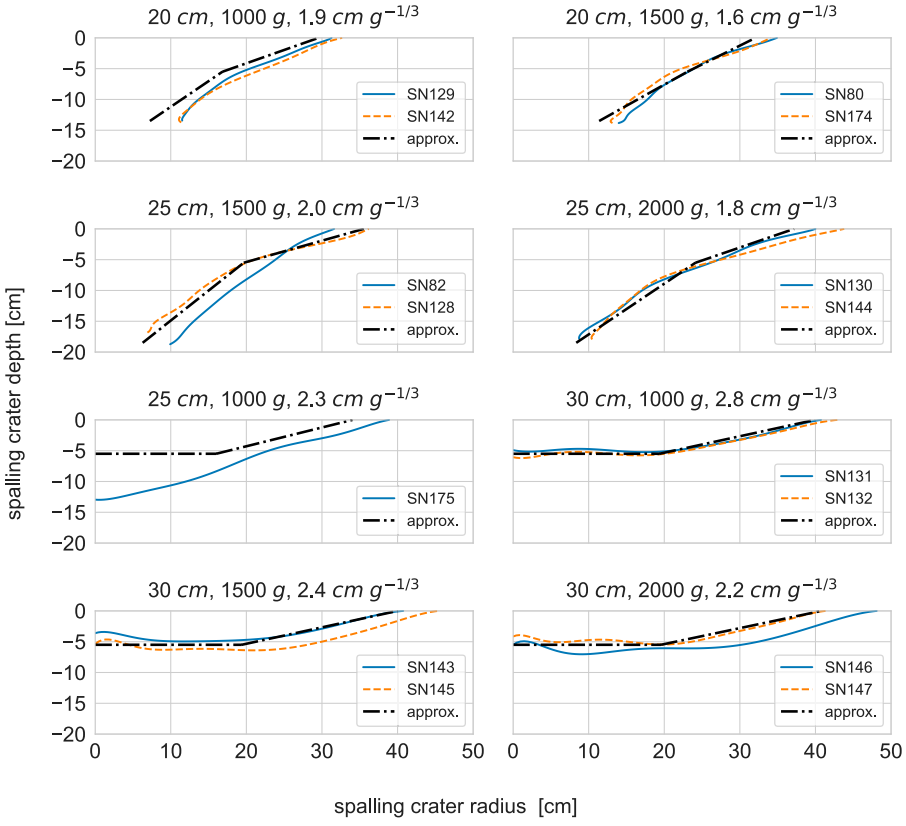

Figure 15. Averaged shapes of the spalling crater for all tests including proposed approximations.

The dash-dotted lines in Figure 15 show the proposed approximations. They are in good agreement with the measured shape of the damaged volume (dashed and solid lines). The only exception is test SN175, in which the depth of the spalling crater is considerably higher than the predicted value. It seems, that this configuration is very close to the transition where a breach occurs. This does not agree with the threshold scaled thickness of 2.2 cm $g^{-1/3}$ for the occurrence of a breach, because SN175 with a scaled thickness of 2.3 cm $g^{-1/3}$ is further away from the threshold than for example SN146 and SN147 (2.2 cm $g^{-1/3}$). The same trend can be observed, when the breach threshold is compared with the values given by UFC 3-340-02 (Figure 11). Therefore, it seems probable that the spalling

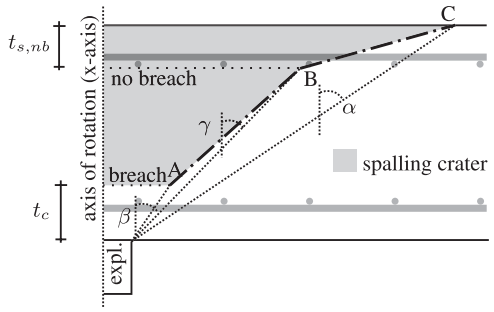

Figure 16. Geometry of the approximation of the spalling crater defined by: radius of the breach (A), radius of the spalling crater at the surface of the concrete slab (C), and radius at the plane of the reinforcement (B).

predicted volume of the spalling crater with the average measured concrete density of 2.22 g cm^{-3}, is shown. For a scaled thickness of 2.3 cm g$^{-1/3}$, the averaged mass ("+") is equal to the measured mass ("-"), because only one test was conducted for this constellation of explosive mass and concrete slab thickness.

Figure 17 (right) shows the size distribution of the spalled debris on the protective side of the concrete slab in context with the occurrence of a breach. These values could be taken from the sieved and weighed debris mass. The influence of the wetness of the spalled debris was acceptable for the size distribution, because the proportions of the different debris sizes are evaluated with relative masses, referring to the total mass of the spalled debris.

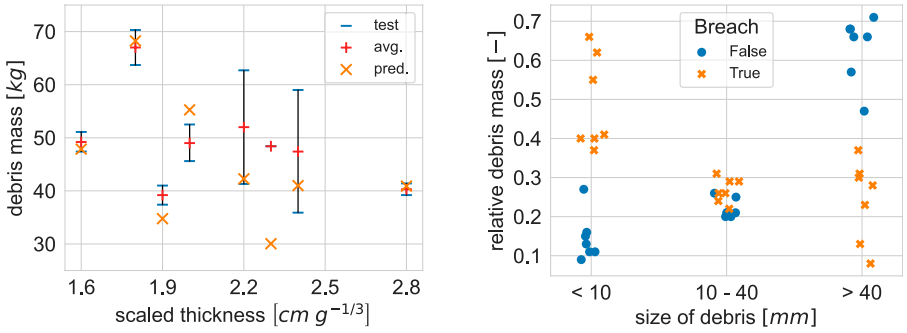

Figure 17. Comparison of the measured spalled debris mass and the predicted spalled debris mass on the protective side of the concrete slab(left), size distribution of the spalled debris on the protective side of the concrete slab(right).

behavior is caused by some other reason like defects in the concrete matrix. To verify this assumption, further tests with a similar constellation of slab thickness and explosive mass would be needed.

Mass of secondary debris

The resulting secondary debris was collected separately for each slab after the associated test. A vacuum cleaner was used for this purpose, to make sure that also very fine debris was collected. During transport and storage some of the debris got wet and could not be used for further evaluation of the total debris mass. Therefore, in the following the total mass of the spalled debris will be calculated based on the volume of the spalling crater which was measured by the 3D-scans, multiplied by the density measured on test cubes of the concrete. Figure 17 (left) shows the determined secondary debris masses on the protective side of the concrete slab for all tests ("-"). These masses are averaged for the same test constellation of explosive mass and concrete slab thickness ("+"). In addition, the predicted debris mass ("x"), which is calculated by multiplying the

In Figure 17 (left) the average difference between the predicted ("×") and the averaged debris mass ("+") of the tests is 16%. When this difference is compared with the average difference of 20% between the tests with the same constellation ("-") for explosive mass and slab thickness, a good correlation can be concluded. For most tests, the predicted debris mass ("×") is within the range of the debris masses measured in the tests ("-"). For a scaled thickness of 2.0 cm g$^{-1/3}$, the predicted debris mass ("×") is 11% above the range of the debris masses measured in the tests ("-"). But this difference is in an acceptable range, when compared with the other presented tests. For the scaled thickness of 2.3 cm g$^{-1/3}$, the measured debris mass ("+" = "-") is noticeably (61%) above the predicted debris mass ("×"). This is caused by the bigger depth of the spalling crater, which was discussed earlier (Figure 15, SN175).

It is unclear, if the part of the crushing crater between the explosive and the breach (Figure 16) has to be added to the secondary debris on the protective side. Or if it ricochets backwards from the surface of the only partially damaged concrete, before the reflected tensile wave reaches the crushing crater and a breach is formed as an opening

between crushing crater and spalling crater. To get further insight into this, numerical simulations will be conducted in a following paper.

From Figure 17 (right) it becomes obvious, that in dependence on the occurrence of a breach the size distribution of the debris changes completely. In case of no breach, ("•") on average ∼60% of the debris has a size bigger than 40 mm and only on average ∼15% has a size smaller than 10 mm. When a breach occurs ("×") this relation flips. With a breach on average ∼50% of the debris has a size smaller than 10 mm and only an average of ∼25% has a size bigger than 40 mm. The debris with a size between 10 and 40 mm has in both cases an average proportion of ∼25%. Parts smaller than 10 mm include the maximum grain size of the concrete and a big proportion of this size range results from a more complete fragmentation of the concrete.

Conclusion and outlook

The conducted tests have been presented and evaluated with the help of regression analysis. The accomplished tracking gives a deeper insight into the flight direction as well as the maximum velocity of the secondary debris.

In the preliminary test series, the originally planned experimental setup has been improved in cooperation with the TNO in The Hague. This test setup includes high-speed recordings of the protective side of the concrete slab, to investigate the formation and flight of the secondary debris.

For the evaluation of the conducted high-speed recordings, a tracking algorithm was developed, which can track the occurring secondary debris, to measure its velocity and flight direction. A quadratic correlation could be observed between the scaled thickness of the concrete slabs and the maximum velocity of the secondary debris in x-direction. The velocity in radial direction is zero at the center of the debris cloud and increases with an increasing radial distance from the center. This increase can be approximated with a linear relation. The radial velocity in the conducted tests was always below 50% of the velocity in x-direction, which equals to an angle of the resulting velocity ($v_x + v_y$) relative to the x-axis smaller than 20°. This shows that the flight direction of the debris is dominant in x-direction.

The damaged concrete slabs were documented with 3D-scans. With a rotational projection of the scanned surface points into one common plane and averaging their location by a higher order polynomial, a new method has been proposed to evaluate the shape of the spalling crater. This method gives a possibility to compare the occurring irregular shapes of the emerging spalling craters.

The new proposed method for the approximation of the spalling crater gives a possibility to predict the total mass of the secondary debris. This method describes the geometry of the spalling crater in dependence on the introduced angles for the description of the diameter of the spalling crater and the diameter of the breach. In the conducted test, these angles are in a range of 47°–57° for the spalling crater angle and a range of 13°–56° for the breach angle. Both angles can be determined by the observed regression lines with respect to the scaled thickness of the concrete slab.

The occurrence of a breach in the conducted tests was compared to the predictions by UFC 3-340-02 (DoD, 2008). A good correlation can be observed. For the proposed model, a scaled thickness smaller than 2.2 cm $g^{-1/3}$ was determined, on the basis of the conducted tests, as the threshold for the occurrence of a breach.

To make predictions about the effects of the secondary debris on humans and installations on the protective side of the concrete slab, the mass-velocity-distribution of the secondary debris is needed. This relation cannot be measured experimentally with the current setup, because the HS-cameras can only record the outer parts of the debris cloud, and there is no correlation between the tracked features and the associated mass of the secondary debris. Therefore, in a next step, numerical simulations will be evaluated for their ability to predict the secondary debris resulting from contact detonations on concrete slabs. Numerical simulations can give a deeper insight into the occurring processes like, for example, the distribution of the velocities over the resulting debris mass.

Declaration of conflicting interests

The authors declare that they have no known competing financial interests or personal relationships that could have appeared to influence the work reported in this paper.

Funding

The author(s) disclosed receipt of the following financial support for the research, authorship, and/or publication of this article: The project is financed by the German Federal Ministry for Economic Affairs and Energy under the project number 1501581.

ORCID iD

Moritz Hupfauf https://orcid.org/0000-0001-7011-0502

References

Bewick B (2017) *Fragmentation of Solid Materials Using Shock Tubes. Part 2 : First Test Tube*. Technical report. Fort Belvoir, VA: Defense Threat Reduction Agency.

Bouguet JY (1999) *Pyramidal Implementation of the Affine Lucas Kanade Feature Tracker Description of the Algorithm*. Austin, TX: Intel Corporation Microprocessor Research Lab.

Department of Defense (2008) Unified Facilities Criteria (UFC): structures to resist the effects of accidental explosions. Technical Report UFC 3-340-02.

Gebbeken N and Krauthammer T (2013) *Understanding the Tensile Properties of Concrete - Understanding the Dynamic Response of Concrete to Loading: Practical Examples*. Amsterdam, Netherlands: Elsevier, 338–364. ISBN 978-0-857-09753-8.

Hartley R and Zisserman A (2004) *Multiple View Geometry in Computer Vision*. Cambridge, UK: Cambridge University Press. ISBN 9780521540513. DOI: 10.1017/CBO9780511811685

Hiermaier S (2008) *Structures under Crash and Impact*. Boston, MA: Springer US. ISBN 978-0-387-73862-8. DOI: 10.1007/978-0-387-73863-5

Kaehler A and Bradski G (2016) *Learning OpenCV 3*. Newton, MA: O'Reilly. ISBN 781491937990.

Li J, Wu C and Hao H (2015) Investigation of ultra-high performance concrete slab and normal strength concrete slab under contact explosion. *Engineering Structures* 102: 395–408. DOI: 10.1016/j.engstruct.2015.08.032

Li J, Wu C, Hao H, et al. (2016) Experimental investigation of ultra-high performance concrete slabs under contact explosions. *International Journal of Impact Engineering* 93: 62–75.

Lucas B and Kanade T (1981) An iterative image registration technique with an application to stereo vision. *Proceedings of the 7th International Joint Conference on Artificial Intelligence* 2: 674–679.

McVay MK (1988) Spall damage of concrete structures (Final Report). Tech. Rep. SL-88-22 (Technical Report): 431.

Meyers MA (1994) *Dynamic Behavior of Materials*. Hoboken, NJ: Wiley. ISBN 9780471582625. DOI: 10.1002/9780470172278

Schreer O (2005) *Stereoanalyse und Bildsynthese*. Berlin, Germany: Springer. ISBN 3-540-23439-X.

Shi Y, Wang J and Cui J (2020) Experimental studies on fragments of reinforced concrete slabs under close-in explosions. *International Journal of Impact Engineering* 144: 103630.

Shirbhate PA and Goel MD (2021) A critical review of TNT equivalence factors for various explosives, lecture notes in civil engineering. In: Saha SK and Mukherjee M (eds) *Recent Advances in Computational Mechanics and Simulations*. Singapore: Springer Singapore, 471–478. ISBN 978-981-15-8138-0.

Szeliski R (2010) *Computer Vision: Algorithms and Applications*. Berlin, Germany: Springer.

Tu H, Fung TC, Tan KH, et al. (2019) An analytical model to predict the compressive damage of concrete plates under contact detonation. *International Journal of Impact Engineering* 134: 103344. DOI: 10.1016/j.ijimpeng.2019.103344

van der Voort MM and Weerheijm J (2013) A statistical description of explosion produced debris dispersion. *International Journal of Impact Engineering* 59: 29–37.